Metastability for the Blume-Capel model with distribution of magnetic anisotropy using different dynamics

Yoh Yamamoto and Kyungwha Park*
Department of Physics, Virginia Tech, Blacksburg, Virginia 24061, USA
(Received 17 February 2013; revised manuscript received 21 June 2013; published 11 July 2013)

We investigate the relaxation time of magnetization or the lifetime of the metastable state for a spin $S = 1$ square-lattice ferromagnetic Blume-Capel model with distribution of magnetic anisotropy (with small variances), using two different dynamics such as Glauber and phonon-assisted dynamics. At each lattice site, the Blume-Capel model allows three spin projections $(+1, 0, -1)$ and a site-dependent magnetic anisotropy parameter. For each dynamic, we examine the low-temperature lifetime in two dynamic regions with different sizes of the critical droplet and at the boundary between the regions, within the single-droplet regime. We compute the average lifetime of the metastable state for a fixed lattice size, using both kinetic Monte Carlo simulations and the absorbing Markov chains method in the zero-temperature limit. We find that for both dynamics the lifetime obeys a modified Arrhenius-like law, where the energy barrier of the metastable state depends on the temperature and standard deviation of the distribution of magnetic anisotropy for a given field and magnetic anisotropy and that an explicit form of this dependence differs in different dynamic regions for different dynamics. Interestingly, the phonon-assisted dynamic prevents transitions between degenerate states, which results in a large increase in the energy barrier at the region boundary compared to that for the Glauber dynamic. However, the introduction of a small distribution of magnetic anisotropy allows the spin system to relax via lower-energy pathways such that the energy barrier greatly decreases. In addition, for the phonon-assisted dynamic, even the prefactor of the lifetime is substantially reduced for a broad distribution of magnetic anisotropy in both regions considered, in contrast to the Glauber dynamic. Our findings show that overall the phonon-assisted dynamic is more significantly affected by the distribution of magnetic anisotropy than the Glauber dynamic.

DOI: 10.1103/PhysRevE.88.012110 PACS number(s): 05.50.+q, 64.60.Q−, 75.60.Jk, 02.50.Ga

I. INTRODUCTION

Metastability is ubiquitous in many physical, chemical, and biolological systems. One of the common examples is metastability occurring in the relaxation of magnetization of a ferromagnetic material in the presence of an external magnetic field. Suppose that a ferromagnetic material is initially prepared with magnetization saturated with a strong magnetic field and that the magnetic field direction is rapidly reversed. Then the state with the reversed magnetization is now the ground state or the stable state. If the thermal energy is much lower than the energy barrier against nucleation of the stable phase, the initial state can have a long lifetime and it becomes a metastable state.

Magnetic nanoparticles, clusters, and molecules are interesting due to their utilization as a tool to explore quantum properties at the nanometer scale by themselves or when they are embedded in different types of substrates or solutions. They also have various applications including information storage devices [1,2], sensors, and contrast agents in magnetic resonance imaging [3–5]. Synthesized magnetic nanoparticles have typically large distributions of size and shape which influence their equilibrium and nonequilibrium properties [6–13]. For example, the size and shape distributions induce distributions in the magnetic anisotropy barrier, magnetization switching or relaxation, and blocking temperature.

To understandnonequilibrium properties of collections of magnetic nanoparticles with size and shape distributions, one needs to go beyond the ferromagnetic Ising model in order to include a nontrivial effect of magnetic anisotropy. The minimal model for this purpose is a spin $S = 1$ ferromagnetic Blume-Capel (BC) model [14,15], which was originally introduced to understand features of the phase diagram of He^3-He^4 mixtures and a phase transition in UO_2. In the BC model, each lattice site can take three possible spin projections $(+1, 0,$ and $-1)$ and magnetic anisotropy favors spin projections of ± 1. A spin $S > 1$ BC model can be applied to arrays of weakly interacting magnetic nanoparticles [16,17], of nanoscale single-molecule magnets such as Mn_{12} and Fe_8 [18–20], and of a $Mn(III)_2Ni(II)$ single-chain magnet [21,22]. Distributions of size and shape of magnetic nanoparticles can be modeled as distributions of magnetic anisotropy at different lattice sites with the magnetic moment at each site fixed [23].

Another crucial factor in the investigation of nonequilibrium properties or magnetization relaxation for magnetic nanoparticles is to select a transition rate or dynamic relevant to the system of interest. In many cases, relaxation of magnetization for magnetic nanoparticles or clusters was studied using the Glauber dynamic [24] without its justification or derivation from a microscopic model, except for a few cases [25,26]. Other commonly used dynamics are Metropolis [27] and soft stochastic dynamics [28]. It has been shown that different dynamics demand even different interpretations of the Arrhenius law [29] as well as different nonequilibrium properties [30] in the Ising model and nanostructures of field-driven solid-on-solid interfaces. One of us derived a transition rate or dynamic from a microscopic

*Electronic address: kyungwha@vt.edu

model where a spin system ($S \geqslant 1$ generalized BC model) is weakly coupled to a d-dimensional phonon bath [31]. A similar transition rate to this was used to estimate the spin-lattice relaxation time in quantum dots [32]. Henceforth, we refer to this dynamic as the d-dimensional phonon-assisted (PA) dynamic. Different dynamics may be affected differently by the distribution of magnetic anisotropy, which could be used to determine the underlying dynamic of the system of interest. So far, the effect of the dynamic on magnetization relaxation with distribution of size (or on the lifetime of the metastable state with distribution of magnetic anisotropy) has not been studied.

In this work, we focus on two aspects of the average lifetime of the metastable state with distribution of magnetic anisotropy within the single-droplet regime in the zero-temperature limit: (i) the effect of transition rate or dynamic and (ii) the effect of dynamic region (with a different size of the critical droplet) and of the boundaries between the regions. We consider the spin $S = 1$ ferromagnetic BC model on a square lattice with distribution of magnetic anisotropy. (In this case, we assume that the magnetic anisotropy parameter has a small variance compared to its mean value.) We apply both the Glauber and the three-dimensional PA dynamics to the BC model in two dynamic regions and at the boundary between the regions. We perform kinetic Monte Carlo simulations (KMCSs) and use the absorbing Markov chains (AMCs) method for a fixed lattice size, and determine the average lifetime in the zero-temperature limit, $\langle\tau\rangle$ $(=Ae^{\beta\Gamma})$, where $\beta = 1/(k_B T)$, k_B is the Boltzmann constant, and T is the temperature. We find that, for both dynamics, the energy barrier Γ depends on the temperature and standard deviation of the distribution of magnetic anisotropy for a given field and magnetic anisotropy and that, for the PA dynamic, even the prefactor A depends on the standard deviation of the distribution of magnetic anisotropy as well as field and magnetic anisotropy for a given region. At the region boundary, without distribution of magnetic anisotropy, the energy barrier Γ for the PA dynamic is much higher than that for the Glauber dynamic due to forbidden transitions between degenerate states. However, with distribution of magnetic anisotropy, the metastable state can relax via low-energy pathways induced by the lowest magnetic anisotropy within the distribution, and the barrier for the PA dynamic is greatly reduced. Overall, the PA dynamic is more susceptible to the distribution of magnetic anisotropy than the Glauber dynamic in the regions and at the boundary considered.

This work is organized as follows. In Sec. II, we discuss the BC model and metastability, and specify two dynamic regions of interest within the single-droplet regime. In Sec. III, we briefly introduce the Glauber and PA dynamics and discuss our implementation of advanced algorithms (such as the n-fold way algorithm and the $s = 2$ Monte Carlo algorithm with absorbing Markov chains (MCAMCs) [33–35]) in KMCSs with constant magnetic anisotropy and distribution of magnetic anisotropy. We also describe the AMC method to calculate the lifetime analytically. In Sec. IV, we present our results from KMCS and the AMC method using the two dynamics for constant magnetic anisotropy and distribution of magnetic anisotropy in the two regions and at the boundary. In Sec. V, we report our conclusions.

II. MODEL

A. Blume-Capel model

We consider the spin $S = 1$ BC model on a square lattice $L \times L$ with periodic boundary conditions [14,15]:

$$\mathcal{H} = -2J \sum_{\langle i,j \rangle} S_{iz} S_{jz} - H \sum_i S_{iz} - D \sum_i S_{iz}^2, \qquad (1)$$

where S_{iz} is the projection of spin at lattice site i onto the magnetic easy axis (z axis). S_{iz} can take three possible eigenvalues $M_{iz} = +1$, 0, and -1. The first term in the model describes exchange interactions between the nearest-neighbor spins at sites i and j with exchange coupling constant J. The second term is the Zeeman energy with external magnetic field H. The last term corresponds to the magnetic anisotropy energy, where $D(>0)$ is a uniaxial magnetic anisotropy parameter. The magnetic anisotropy energy arises from perturbative treatment of spin-orbit coupling [36], and the magnetic anisotropy barrier for the BC model is DS^2. The $S = 1$ BC model is the simplest case where the magnetic anisotropy energy nontrivially contributes to the total energy. Equilibrium ground-state spin configurations for the BC model (with constant D) at zero temperature were shown in Ref. [23]. For $(-D - 4) < H$ and $H > 0$, the configuration of all sites with $M_z = 1$ is the ground state. The critical temperature T_c of the BC model increases with increasing D/J at $H = 0$ [37]. The value of T_c for $D = 0$ was calculated using various methods [38–40]. To simulate the size distribution, we consider a distribution of D over the lattice sites (D_i) with a fixed spin or magnetic moment per site. Henceforth, we use J as units of energy.

B. Decay of the metastable state for the Blume-Capel model

For the Ising model on a square lattice, decays of the metastable state and nucleation of droplets of the stable phase have been extensively studied as a function of $|H|$, T, and L [35,41–44]. For the BC model on a square lattice, nucleation and metastability were studied at low fields in a multidroplet regime using the Metropolis transition rate [45], and nonequilibrium short-time dynamics at T_c were investigated using the Glauber transition rate [37]. Here we are interested in low-temperature decays of the metastable state using both the Glauber and the PA transition rates, within the single-droplet regime, for the BC model for a fixed lattice size L, where the size of the critical droplet of the stable phase is much smaller than the lattice size. The lifetime of the metastable state is defined to be the time at which the magnetization of the BC model becomes 0. For a fixed lattice size and constant D, when we take a zero-temperature limit, the single-droplet regime falls on the region defined by $|H| < (D + 4)$ [23]. We divide the single-droplet regime into different regions according to the critical droplet size. For example, for $0 < D < 1$, at fields that are not too low, three regions, labeled I, II, and III, are identified as a function of $|H|$ and D (Fig. 1). (Regions I-A, I-B, and I-C are considered region I.) The critical droplet for region I is a single site of spin projection $M_z = 0$. Region I has three subregions where prefactor A in $\langle\tau\rangle$ for the Glauber dynamic (for constant D)

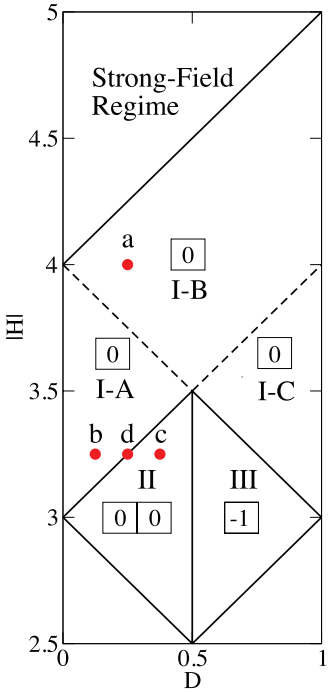

FIG. 1. (Color online) Cross-over dynamic "phase" diagram for metastable decay for the square-lattice ferromagnetic BC model with $0 < D < 1$ in the zero-temperature limit (for constant D). Three regions or dynamic phases within the single-droplet regime I, II, and III are specified. The thick solid lines divide different regions, and the dashed lines divide sub-regions in the region I such as I-A, I-B, and I-C. For each region, critical droplets are illustrated. Exceptions are the boundaries between different regions for the PA dynamic. The three points marked as b–d are investigated in this work, while the point a was studied in Ref. [23].

changes: $A = 9/8$ for region I-A ($3 + D < |H| < 4 - D$ for $D > 0$), $A = 10/9$ for region I-B ($4 - D < |H| < 4 + D$ for $0 < D < 0.5$ and $3 + D < |H| < 4 + D$ for $D > 0.5$), and $A = 2$ for region I-C ($4 - D < |H| < 3 + D$ for $D > 0.5$). The critical droplet for region II ($3 - D < |H| < 3 + D$ for $D < 0.5$) consists of two nearest-neighbor sites with each spin projection $M_z = 0$. The critical droplet for region III ($2 + D < |H| < 4 - D$ for $D > 0.5$) is a single site of spin projection $M_z = -1$. For regions II and III, there are no such subregions as in region I. Previously, we investigated the case with $H = -4$ and $D = 0.25$ (marked as a in =region I-B in Fig. 1), using the Glauber dynamic [23]. In the current work, we focus on metastability in the regions I-A and II and at the boundary ($|H| = D + 3$ and $0 < D < 0.5$) between those regions. More specifically, we vary D with H fixed as -3.25: $D = 0.125$ for the region I-A, $D = 0.375$ for the region II, and $D = 0.25$ for the boundary as marked b, c, and d in Fig. 1. We do not further consider regions with lower magnetic fields because (i) a similar rationale to our current study can be applied to those regions, and (ii) a larger number of transient states is required to apply the AMC method and MCAMC to those regions, which brings complexity to analytical forms and KMCS data and obscures our main findings. Interested readers are referred to the Appendix, where an analytical form of $\langle \tau \rangle$ is provided in region IV-A [$(2 + D) < |H| < (3 - D)$ and $D > 0$] using the Glauber dynamic for constant D and distribution of D.

III. METHODS AND ALGORITHMS

We use KMCS and the AMC method to compute the average lifetime of the metastable state. In our KMCS, we use $L = 40$ and update a spin configuration via a single spin flip at randomly selected site i with $\Delta M_z = \pm 1$, using either the Glauber or the PA dynamic. The spin-flip probability using the Glauber dynamic p_g is given by

$$p_g = \frac{1}{1 + e^{\beta \Delta E}}, \tag{2}$$

where $\Delta E = E_{\rm new} - E_{\rm old}$. Here $E_{\rm old}$ ($E_{\rm new}$) is the total energy of the spin system before (after) a single spin flip at site i. The PA transition rate [31] is given by

$$W_{\rm pa} = \alpha \left| \frac{(\Delta E)^3}{1 - e^{-\beta \Delta E}} \right|, \tag{3}$$

where α is a material-dependent parameter which does not depend on ΔE. For example, for the single-molecule magnet Mn_{12}, $\alpha = 0.00041\ {\rm s}^{-1}$ [31]. In our KMCS, we set $\alpha = 1$, and the spin-flip probability for the PA dynamic is identical to $W_{\rm pa}$.

In the standard dynamic Monte Carlo algorithm, a simulated physical time in units of Monte Carlo steps per spin is proportional to a CPU time for a fixed lattice size. For the parameters of our interest, a decay of the metastable state would take an extremely long CPU time if the standard algorithm were used, due to the long time required to exit the initial state at low temperatures. To circumvent this problem, we use the following advanced algorithms, where an exit time from the current spin configuration is calculated and the simulation time (in units of Monte Carlo steps) is set to this time. For constant D, we first use the $s = 2$ (two transient states) MCAMC [35] until the system exits from the transient subspace and then use the n-fold way algorithm [33,34] for discrete time. In the $s = 2$ MCAMC algorithm, the first transient state is the initial state, and the second transient state is all N spin configurations of spin projection $M_z = 0$ at a single site from the initial state. With distributions of D, we first use the n-fold way algorithm (a modified version to accommodate different values of D at different lattice sites), until the system exits from the initial state, and then use the standard Monte Carlo algorithm in our KMCS. For analytic calculations of the average lifetime, we apply the $s = 3$ AMC method (three transient states) and take the zero-temperature limit.

A. *n*-fold way algorithm for three-state systems with constant *D*

The n-fold way algorithm proposed in Refs. [33] and [34] was successfully used for the Ising model on a square lattice. In the algorithm, all spins on the lattice are classified into 10 classes according to spin orientation (up or down) and the sum of the four nearest-neighbor spin orientations. To apply this algorithm to the BC model, modifications are needed. For the BC model, all spins are now classified into 27 classes based on the spin projection ($+1$, 0, or -1) and the sum of the four nearest-neighbor spin projections (0, ± 1, ± 2, ± 3, or ± 4). The 27 classes are listed with ΔE in Table I.

TABLE I. The 27 spin classes for the BC model on a square lattice. For classes 19–27 two different values of ΔE are listed: the first is for $M_z = 0 \to +1$, and the second for $M_z = 0 \to -1$.

Class No.	Spin projection	Sum of nearest-neighbor spin projections	$\Delta E = E_{\text{new}} - E_{\text{old}}$
1	+1	+4	$4 - \|H\| + D$
2	+1	+3	$3 - \|H\| + D$
3	+1	+2	$2 - \|H\| + D$
4	+1	+1	$1 - \|H\| + D$
5	+1	0	$-\|H\| + D$
6	+1	−1	$-1 - \|H\| + D$
7	+1	−2	$-2 - \|H\| + D$
8	+1	−3	$-3 - \|H\| + D$
9	+1	−4	$-4 - \|H\| + D$
10	−1	+4	$-4 + \|H\| + D$
11	−1	+3	$-3 + \|H\| + D$
12	−1	+2	$-2 + \|H\| + D$
13	−1	+1	$-1 + \|H\| + D$
14	−1	0	$\|H\| + D$
15	−1	−1	$1 + \|H\| + D$
16	−1	−2	$2 + \|H\| + D$
17	−1	−3	$3 + \|H\| + D$
18	−1	−4	$4 + \|H\| + D$
19	0	+4	$-4 + \|H\| - D$ or $4 - \|H\| - D$
20	0	+3	$-3 + \|H\| - D$ or $3 - \|H\| - D$
21	0	+2	$-2 + \|H\| - D$ or $2 - \|H\| - D$
22	0	+1	$-1 + \|H\| - D$ or $1 - \|H\| - D$
23	0	0	$\|H\| - D$ or $-\|H\| - D$
24	0	−1	$1 + \|H\| - D$ or $-1 - \|H\| - D$
25	0	−2	$2 + \|H\| - D$ or $-2 - \|H\| - D$
26	0	−3	$3 + \|H\| - D$ or $-3 - \|H\| - D$
27	0	−4	$4 + \|H\| - D$ or $-4 - \|H\| - D$

Another subtlety is that each of classes 19–27 (a lattice site with $M_z = 0$) has two possibilities for a single spin flip, such as either $M_z = +1$ or $M_z = -1$, each of which has a different energy change ΔE. Thus, for classes 19–27, we introduce the probability of flipping a spin in class i as $p_i = (p_i^+ + p_i^-)/2$, where $p_i^+ = p_i(M_z = 0 \to 1)$ and $p_i^- = p_i(M_z = 0 \to -1)$. Similarly to the case of the Ising model [35], a quantity Q_i is defined to calculate a discrete time to exit from the current spin configuration,

$$Q_i = \frac{1}{N} \sum_{j=1}^{i} n_j p_j, \quad 1 \leqslant i \leqslant 27, \tag{4}$$

where $Q_0 = 0, n_j$ is the number of spins or lattice sites in class j, and $N = L^2$. Following the scheme used in the standard n-fold way algorithm, the exit time m from the current spin configuration is given by

$$m = \left\lfloor \frac{\ln(\bar{r})}{\ln(1 - Q_{27})} \right\rfloor + 1, \tag{5}$$

where $\bar{r}$ is a random number and $\lfloor x \rfloor$ is the integer part of x.

B. *n*-fold way algorithm for distributions of *D*

With distributions of D, one must treat every lattice site individually to reflect the randomness of D. Hence, we classify all spins into N classes according to the lattice site rather than the 27 spin classes. Then we define a quantity Q_i as follows:

$$Q_i = \frac{1}{N} \sum_{j=1}^{i} p_j, \quad 1 \leqslant i \leqslant N, \tag{6}$$

where $Q_0 = 0$. The exit time m from the current spin configuration is now

$$m = \left\lfloor \frac{\ln(\bar{r})}{\ln(1 - Q_N)} \right\rfloor + 1. \tag{7}$$

In this case, one needs to update p_j due to randomness of D in order to calculate the exit time m rather than updating n_j for constant D in Eq. (4). This algorithm is not efficient because a memory allocation time depends on the system size N. Therefore, we switch to the standard Monte Carlo algorithm once the spin system exits from the initial state.

C. AMC method

To analytically calculate the average lifetime for constant D, we use the $s = 3$ AMC method with three transient states. For region I-A, the $s = 2$ AMC method can also be used, but for region II, we must use the $s = 3$ AMC method. The magnetization of the spin system reaches 0 shortly after a critical droplet is formed in the single-droplet regime. Hence, the average lifetime is approximately the exit time from the transient subspace in the AMC. Using the transient states and

several absorbing states, we create a transition matrix for the AMC and find an analytic form for the exit time. For details of the AMC method, see Ref. [35]. In the $T \to 0$ limit, we expect that the analytic form should be a good approximation to the average lifetime from our KMCS. For Gaussian distributions of D, we first calculate an average of each relevant spin-flip probability by integrating the probability over D and then use the averages in the analytic form of the exit time for constant D [23]. In this case, we assume that N is so large that a summation over the lattice sites approximates an integral. Thus, we expect that the finite-size effect is more prominent for larger σ_D [23].

IV. RESULTS: CONSTANT MAGNETIC ANISOTROPY PARAMETER

We present analytic and simulated average lifetimes $\langle\tau\rangle$ in regions I-A and II and at the boundary for constant D (specifically the parameter values labeled b–d in Fig. 1), using the Glauber dynamic. Then a similar analysis is carried out for the PA dynamic. In our KMCS, 2000 escapes are simulated for a thermal average at a given value of β.

The highlights of our results in this section are as follows. The energy barrier Γ in $\langle\tau\rangle$ increases with increasing D for a fixed $|H|$. The increase in region II is greater than in region I-A for both dynamics. At the boundary, the barrier Γ for the PA dynamic greatly increases compared to the Glauber dynamic due to forbidden transitions under the PA dynamic. The prefactor A in $\langle\tau\rangle$ for the Glauber dynamic is constant for a given region, but it is different at the boundary. The prefactor A for the PA dynamic, however, depends on D and $|H|$ even for a given region.

To calculate the analytic form of the lifetime, we use the $s = 3$ AMC method with the following three transient states (and five absorbing states): (i) the initial state, (ii) the state of a single site with $M_z = 0$ from the initial state (N possible configurations), and (iii) the state of two nearest-neighbor sites with each spin $M_z = 0$ from the initial state ($2N$ possible configurations). The exit time from the transient subspace or $\langle\tau\rangle$ as a function of $|H|$, D, T, and N is given by

$$\begin{aligned}
\langle\tau\rangle &= \frac{F_1(p_1) + F_2(p_1) + F_0 + p_{19}^{+}(6p_2 + p_{20}^{+} + p_{20}^{-})}{p_1[F_3(p_1) + F_4(p_1) + F_0]},\\
F_0 &= 48p_2^2 + p_{19}^{-}(p_{20}^{+} + p_{20}^{-}) + p_2(6p_{19}^{-} + 8p_{20}^{-}),\\
F_1(p_1) &= p_1^2(80 - 42N + 4N^2),\\
F_2(p_1) &= p_1[(40N - 124)p_2 + (N - 8)(p_{19}^{+} + p_{19}^{-})\\
&\quad + (4N - 10)(p_{20}^{+} + p_{20}^{-})],\\
F_3(p_1) &= 2p_1^2(40 - 13N + N^2),\\
F_4(p_1) &= p_1[(20N - 124)p_2 + (N - 8)p_{19}^{-}\\
&\quad + (2N - 10)(p_{20}^{+} + p_{20}^{-})],
\end{aligned} \tag{8}$$

where p_i is a spin-flip probability in spin class i listed in Table I. Equation (8) is valid in regions I-A and II and the region boundary for the Glauber dynamic and in regions I-A and II for the PA dynamic, because the critical droplets for regions I-A and II are included in the transient subspace for both dynamics. However, Eq. (8) is *not* valid at the boundary for the PA dynamic. Further discussion follows.

A. Glauber dynamic

For the Glauber dynamic, p_i's in Eq. (8) are written as

$$p_1 = \frac{1}{1 + e^{\beta(4+D-|H|)}}, \quad p_2 = \frac{1}{1 + e^{\beta(3+D-|H|)}}, \tag{9}$$

$$p_{19}^{+} = \frac{1}{1 + e^{\beta(-4-D+|H|)}}, \quad p_{20}^{+} = \frac{1}{1 + e^{\beta(-3-D+|H|)}}, \tag{10}$$

$$p_{19}^{-} = \frac{1}{1 + e^{\beta(4-D-|H|)}}, \quad p_{20}^{-} = \frac{1}{1 + e^{\beta(3-D-|H|)}}. \tag{11}$$

Let us first present our result for region I-A ($3 + D < |H| < 4 - D$ and $D > 0$). In the $T \to 0$ limit, p_1 becomes $\exp[-\beta(4 + D - |H|)]$, while p_2, p_{19}^{+}, and p_{20}^{-} approximate unity. In addition, p_{19}^{-} and p_{20}^{+} approximate $\exp[-\beta(4 - D - |H|)]$ and $\exp[\beta(3 + D - |H|)]$, respectively, and so they vanish in the zero-temperature limit. Thus, the average lifetime, Eq. (8), in the zero-temperature limit becomes

$$\langle\tau\rangle = \frac{8p_2 + p_{19}^{+}}{8p_1p_2} = \frac{A}{p_1} = Ae^{\beta\Gamma(D,H)}, \tag{12}$$

where $\Gamma(D,H) = 4 + D - |H|$ and $A = 9/8$ is independent of D and $|H|$ in region I-A. Simulations are performed using the $s = 2$ MCAMC for $L = 40$, $D = 0.125$, and $|H| = 3.25$ in the range of $\beta = 50$–690 (Fig. 2). We use two methods to fit the KMCS data to Eq. (12): (i) to use A and Γ as fitting parameters and (ii) to use only A as a fitting parameter with Γ fixed as the value from the $s = 3$ AMC method ($\Gamma = 0.875$). The first method provides that $\Gamma = 0.8750 \pm 1.53 \times 10^{-5}$ and $A = 1.1246 \pm 0.0071$, while the second method gives $A = 1.1221 \pm 0.0032$. The fitted values agree with the analytic values, $\Gamma = 0.875$ and $A = 1.125$, within the uncertainties.

We now present our result for region II ($3 - D < |H| < 3 + D$ and $D < 0.5$). In the $T \to 0$ limit, p_1 and p_2 become $\exp[-\beta(4 + D - |H|)]$ and $\exp[-\beta(3 + D - |H|)]$, respectively. p_{19}^{+}, p_{20}^{+}, and p_{20}^{-} approximate to unity. p_{19}^{-}

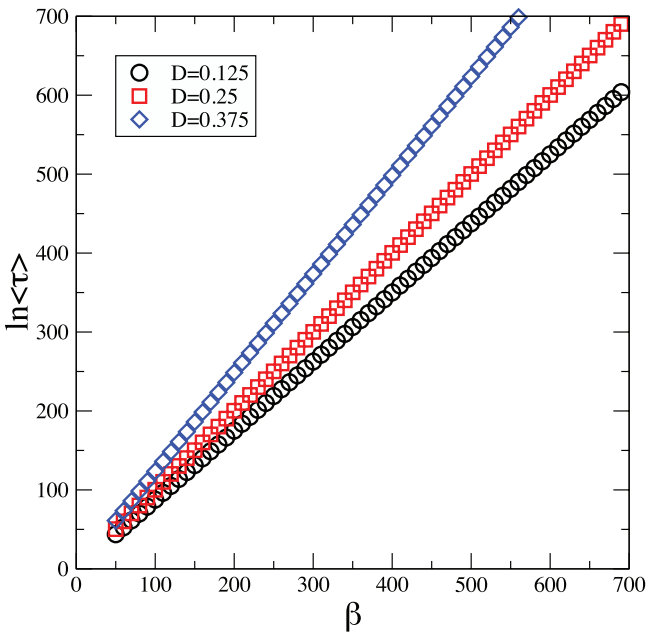

FIG. 2. (Color online) Simulated $\langle\tau\rangle$ vs β using the Glauber dynamic for three constant values of D at $|H| = 3.25$ for $L = 40$.

TABLE II. Fitting of our KMCS data using the Glauber dynamic for constant D at $|H| = 3.25$. In the first method Γ and A are parameters, and in the second method only A is fitted.

Method	Region I-A ($D = 0.125$)	Boundary ($D = 0.25$)	Region II ($D = 0.375$)
First	$\Gamma = 0.8750 \pm 1.53 \times 10^{-5}$	$\Gamma = 1.0000 \pm 1.73 \times 10^{-5}$	$\Gamma = 1.2500 \pm 1.81 \times 10^{-5}$
	$A = 1.1246 \pm 0.0071$	$A = 1.2885 \pm 0.0092$	$A = 0.2486 \pm 0.0015$
Second	$\Gamma = 0.875$ (fixed)	$\Gamma = 1$ (fixed)	$\Gamma = 1.25$ (fixed)
	$A = 1.1221 \pm 0.0032$	$A = 1.2873 \pm 0.0041$	$A = 0.2497 \pm 0.0007$
AMC	$\Gamma = 0.875$	$\Gamma = 1$	$\Gamma = 1.25$
	$A = 1.125$	$A = 1.28125$	$A = 0.25$

approximates $\exp[-\beta(4 - D - |H|)]$, which vanishes as $T \to 0$. The lifetime, Eq. (8), in the zero-temperature limit becomes

$$\langle \tau \rangle = \frac{p_{19}^{+}(p_{20}^{+} + p_{20}^{-})}{8 p_1 p_2 p_{20}^{-}} = \frac{A}{p_1 p_2} = A e^{\beta \Gamma(D,H)}, \tag{13}$$

where $\Gamma(D,H) = 7 + 2D - 2|H|$ and $A = 1/4$. The barrier Γ increases with increasing D more rapidly than in region I-A for a given value of $|H|$. We perform KMCS at $|H| = 3.25$ and $D = 0.375$ in the range $\beta = 50$–560 (Fig. 2). Fitting of our simulation data to Eq. (13) shows that $A = 0.2486 \pm 0.0015$ and $\Gamma = 1.2500 \pm 1.81 \times 10^{-5}$ using the first method and that $A = 0.2497 \pm 0.0007$ using the second method. These values agree with those from the $s = 3$ AMC method ($\Gamma = 1.25$, $A = 0.25$) within the uncertainties.

Finally, we show our result for the boundary between region I-A and region II ($|H| = 3 + D$ and $0 < D < 0.5$). In the $T \to 0$ limit, $p_1 \to \exp[-\beta(4 + D - |H|)]$, p_{19}^{+}, $p_{20}^{-} \to 1$, $p_{19}^{-} \to \exp[-\beta(4 - D - |H|)]$, and p_2, $p_{20}^{+} \to 1/2$. At the boundary, the lifetime is

$$\begin{aligned} \langle \tau \rangle &= \frac{(8p_2 + p_{19}^{+})(6p_2 + p_{20}^{-}) + p_{19}^{+} p_{20}^{+}}{8 p_1 p_2 (6p_2 + p_{20}^{-})} \\ &= A e^{\beta \Gamma(D,H)}, \end{aligned} \tag{14}$$

where $\Gamma = 1$ and $A = 41/32$. In this case, the barrier Γ does not depend on D or $|H|$. The prefactor A differs from that for region I-A or II, because in the zero-temperature limit, p_2 and p_{20}^{+} differ from those for region I-A or II. Fitting of our simulation data in the range of $\beta = 50$–690 (Fig. 2) provides that $\Gamma = 1.0000 \pm 1.73 \times 10^{-5}$ and $A = 1.2885 \pm 0.0092$ using the first method and that $A = 1.2873 \pm 0.0041$ using the second method. These values agree with those from the AMC method within the uncertainties. See Table II for a summary.

B. Phonon-assisted dynamic

For the PA dynamic, p_i's in Eq. (8) are given as

$$p_1 = \frac{(4 + D - |H|)^3}{e^{\beta(4+D-|H|)} - 1}, \quad p_2 = \frac{(3 + D - |H|)^3}{e^{\beta(3+D-|H|)} - 1}, \tag{15}$$

$$p_{19}^{+} = \frac{(-4 - D + |H|)^3}{e^{\beta(-4-D+|H|)} - 1}, \quad p_{20}^{+} = \frac{(-3 - D + |H|)^3}{e^{\beta(-3-D+|H|)} - 1}, \tag{16}$$

$$p_{19}^{-} = \frac{(4 - D - |H|)^3}{e^{\beta(4-D-|H|)} - 1}, \quad p_{20}^{-} = \frac{(3 - D - |H|)^3}{e^{\beta(3-D-|H|)} - 1}. \tag{17}$$

We first present our result for region I-A. In the $T \to 0$ limit, p_1 approximates $(4 + D - |H|)^3 \exp[-\beta(4 + D - |H|)]$. p_2, p_{19}^{+}, and p_{20}^{-} approximate $(-3 - D + |H|)^3$, $(4 + D - |H|)^3$, and $(-3 + D + |H|)^3$, respectively. p_{19}^{-} and p_{20}^{+} approximate $(4 - D - |H|)^3 \exp[-\beta(4 - D - |H|)]$ and $(-3 - D + |H|)^3 \exp[-\beta(-3 - D + |H|)]$, respectively, and they vanish in the zero-temperature limit. Hence, the prefactor and the barrier in Eq. (8) or Eq. (12) are given by

$$\begin{aligned} A &= \frac{8(-3 - D + |H|)^3 + (4 + D - |H|)^3}{8(4 + D - |H|)^3(-3 - D + |H|)^3}, \\ \Gamma &= 4 + D - |H|. \end{aligned} \tag{18}$$

The energy barrier Γ is the same for both dynamics, but the prefactor A is now a function of D and $|H|$ for region I-A, which is not the case for the Glauber dynamic. As $|H|$ becomes close to $3 + D$, the prefactor A dramatically increases. We carry out KMCS at $|H| = 3.25$ and $D = 0.125$ in the range of $\beta = 50 - 690$ (Fig. 3). Fitting of the data provides that $\Gamma = 0.8750 \pm 1.63 \times 10^{-5}$ and $A = 65.0899 \pm 0.4396$ using the first method and that $A = 65.6062 \pm 0.2015$ using the second method. Within the uncertainties, these values agree with those from Eq. (18), $\Gamma = 0.875$ and $A = 65.4927$.

We now examine analytic and simulated lifetimes for region II. In the limit of $T \to 0$, $p_1 \to (4 + D - |H|)^3 \exp[-\beta(4 + D - |H|)]$, and $p_2 \to (3 + D - |H|)^3$

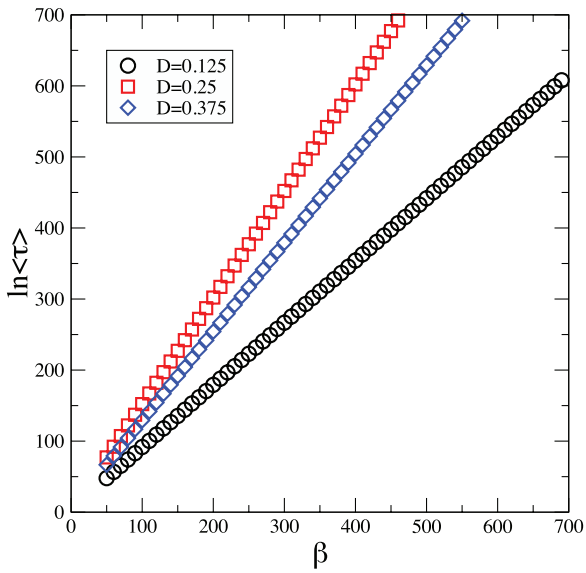

FIG. 3. (Color online) Simulated $\langle \tau \rangle$ vs β using the PA dynamic for three values of D at $|H| = 3.25$ for $L = 40$.

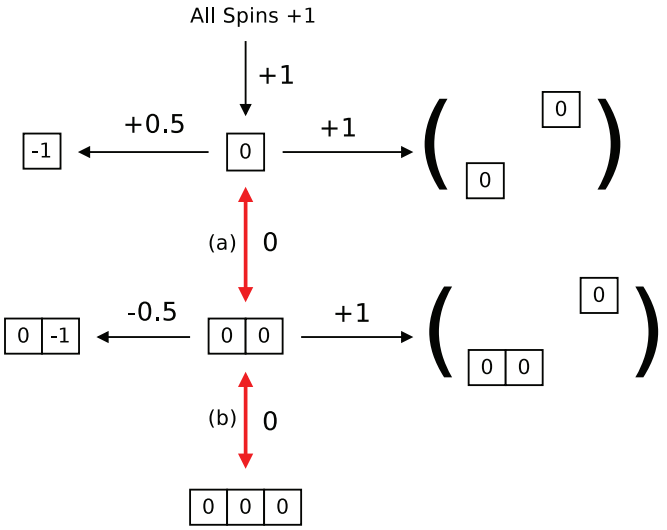

FIG. 4. (Color online) Schematic of relaxation pathways at the region boundary. Each spin configuration shows only flipped spin projections from the initial state. The rightmost upper configuration indicates a state of two non-nearest-neighbor spin projections with each $M_z = 0$. Transitions (a) and (b) are not permitted under the PA dynamic. Numbers next to or above the arrows represent ΔE values between the states for $|H| = 3.25$ and $D = 0.25$.

$\exp[-\beta(3 + D - |H|)]$. $p_{19}^- \to 0$, and p_{19}^+, p_{20}^+, and p_{20}^- approximate $(4 + D - |H|)^3$, $(3 + D - |H|)^3$, and $(-3 + D + |H|)^3$, respectively. Thus, the prefactor and the barrier in Eq. (8) or Eq. (13) are given by

$$A = \frac{(3 + D - |H|)^3 + (-3 + D + |H|)^3}{8(3 + D - |H|)^3(-3 + D + |H|)^3},$$
$$\Gamma = 7 + 2D - 2|H|, \tag{19}$$

where, as $|H|$ becomes close to $3 - D$ or $3 + D$ (boundaries of region II), A greatly increases. For $|H| = 3.25$ and $D = 0.375$, Eq. (19) reveals that $\Gamma = 1.25$ and $A = 64.512$. Fitting our data in the range of $\beta = 50$–550 (Fig. 3) shows that $\Gamma = 1.2500 \pm 2.01 \times 10^{-5}$ and $A = 64.2807 \pm 0.4325$ using the first method and that $A = 64.4455 \pm 0.1894$ using the second method.

Finally, we discuss the average lifetime at the boundary. In this case, interestingly, the transitions labeled (a) and (b) in Fig. 4 are forbidden ($p_2 = 0$, $p_{20}^+ = 0$) because the states involved with the transitions are degenerate. Thus, at the boundary, the critical droplet is now a single site with spin projection $M_z = -1$. This change necessitates the use of a different set of transient states in the $s = 3$ AMC method. The new set of three transient states is the first two transient states, (i) and (ii), discussed earlier and the state of a single site with spin projection $M_z = -1$ from the initial state (N possible configurations). Using this new set in the $s = 3$ AMC method, we find the average lifetime as a function of D, $|H|$, T, and N, as

$$\langle \tau \rangle = \frac{G_1(p_1) + G_2(p_1) + G_0 + p_{19}^+(4p_3 + p_{10})}{p_1(G_3(p_1) + G_0)},$$
$$G_0 = 4\{2p_{10}p_2 + (8p_2 + p_{19}^-)p_3\},$$
$$G_1(p_1) = p_1^2(50 - 30N + 4N^2),$$
$$G_2(p_1) = p_1[(4N - 10)p_{10} + (N - 5)(8p_2 + p_{19}^+) + (2N - 5)(8p_3 + p_{19}^-)],$$
$$G_3(p_1) = 2p_1^2(N - 5)^2 + p_1(N - 5) \times (8p_2 + 8p_3 + 2p_{10} + p_{19}^-), \tag{20}$$

where p_3 and p_{10} are given by

$$p_3 = \frac{(2 + D - |H|)^3}{1 - e^{-\beta(2+D-|H|)}},$$
$$p_{10} = \frac{(-4 + D + |H|)^3}{1 - e^{-\beta(-4+D+|H|)}}. \tag{21}$$

In the zero-temperature limit, p_1 and p_{19}^- are approximately $(4 + D - |H|)^3 \exp[-\beta(4 + D - |H|)]$ and $(4 - D - |H|)^3 \exp[-\beta(4 - D - |H|)]$, respectively. p_3, p_{10}, and p_{19}^+ are close to $(-2 - D + |H|)^3$, $(4 - D - |H|)^3$, and $(4 + D - |H|)^3$, respectively. Note that $p_2, p_{20}^+ \to 0$ as $T \to 0$. Then the lifetime, Eq. (20), in the zero-temperature limit becomes

$$\langle \tau \rangle = \frac{p_{19}^+(4p_3 + p_{10})}{4p_1p_3p_{19}^-} = Ae^{\beta\Gamma}, \tag{22}$$
$$A = \frac{4(-2 - D + |H|)^3 + (4 - D - |H|)^3}{4(-2 - D + |H|)^3(4 - D - |H|)^3},$$
$$\Gamma = 8 - 2|H|. \tag{23}$$

Fitting of our KMCS data for $|H| = 3.25$ and $D = 0.25$, in the range of $\beta = 50$–460 (Fig. 3), shows that $\Gamma = 1.5000 \pm 2.74 \times 10^{-5}$ and $A = 8.2407 \pm 0.0682$ using the first method and that $A = 8.2400 \pm 0.0271$ using the second method. The AMC method gives rise to $\Gamma = 1.5$ and $A = 8.25$. The simulated and analytic results agree within the uncertainties. For a summary, see Table III. At the boundary, the energy barrier for the PA dynamic is much higher than that for the Glauber dynamic, due to the forbidden transitions. A similar increase in the barrier for the PA dynamic (due to forbidden transitions) was discussed for the boundary between region I-C and region III, such as $|H| = 4 - D$ ($0.5 < D < 1$) in Ref. [31].

TABLE III. Fitting of our KMCS data using the PA dynamic for constant D at $|H| = 3.25$.

Method	Region I-A ($D = 0.125$)	Boundary ($D = 0.25$)	Region II ($D = 0.375$)
First	$\Gamma = 0.8750 \pm 1.63 \times 10^{-5}$	$\Gamma = 1.5000 \pm 2.74 \times 10^{-5}$	$\Gamma = 1.2500 \pm 2.01 \times 10^{-5}$
	$A = 65.0899 \pm 0.4396$	$A = 8.2407 \pm 0.0682$	$A = 64.2807 \pm 0.4325$
Second	$\Gamma = 0.875$ (fixed)	$\Gamma = 1.5$ (fixed)	$\Gamma = 1.25$ (fixed)
	$A = 65.6062 \pm 0.2015$	$A = 8.2400 \pm 0.0271$	$A = 64.4455 \pm 0.1894$
AMC	$\Gamma = 0.875$	$\Gamma = 1.5$	$\Gamma = 1.25$
	$A = 65.4927$	$A = 8.25$	$A = 64.512$

V. RESULTS: DISTRIBUTIONS OF THE MAGNETIC ANISOTROPY PARAMETER

We consider Gaussian distributions of D centered at three values of D_0 (0.125, 0.25, and 0.375, shown in Fig. 1) with two values of standard deviation, $\sigma_D = 0.0125$ and 0.025. To generate random numbers with Gaussian distributions, the Box-Muller transformation [46] is used. At a given β and σ_D, 2000 escapes are simulated for a thermal average, and 10 Gaussian distributions are generated for an average over distribution. The same sets of distributions are used for our studies in regions I-A and II and at the boundary for both the Glauber and the PA dynamics. Our results are valid in the case of $\sigma/D \ll 1$. Large variances might strongly influence the low-temperature behavior of the relaxation time [47].

We first discuss our results for the Glauber dynamic and compare them with those for constant D. We then similarly analyze our data for the PA dynamic. The highlights of our results are as follows. For both dynamics, compared to the case for constant D, the average lifetime decreases with Gaussian distributions of D in the two regions and at the boundary, because the barrier Γ decreases with increasing σ_D for a fixed value of β. For a given β and σ_D, both dynamics show that a decrease in the barrier or the lifetime is more apparent in region II than in region I-A. At the boundary, with distributions of D, the PA dynamic now finds lower-energy relaxation pathways so that the lifetime decreases by about 10 orders of magnitude at the low temperatures considered compared to that for constant D (a much greater decrease than for the Glauber dynamic). For the Glauber dynamic, the prefactor A does not change with distribution of D compared to that for constant D. However, for the PA dynamic, the prefactor A depends on even σ_D, and it significantly decreases compared to that for constant D except for the boundary. The decrease is more prominent in region II than in region I-A. For the PA dynamic, at the boundary, the prefactor A greatly increases compared to that for constant D.

A. Glauber dynamic

We present our result for region I-A. To find an analytic form of $\langle\tau\rangle$ with a distribution of D, we first take the zero-temperature limit of the spin-flip probability p_1 in Eq. (9) and then compute the average of the probability over a Gaussian distribution of D, $f(D)$, such as $p_1 = \int f(D)\exp[-\beta(4 + D - |H|)]dD$. Applying this average to Eq. (12), we find the average lifetime as

$$\langle\tau\rangle = A\exp[\beta\Gamma(\beta,H,D_0,\sigma_D)],$$
$$\Gamma(\beta,H,D_0,\sigma_D) = \Gamma_0(H,D_0) - \frac{\beta{\sigma_D}^2}{2}, \tag{24}$$

where $\Gamma_0(H,D_0) = 4 + D_0 - |H|$ and $A = 9/8$. The prefactor A is not affected by $f(D)$. However, due to the correction term in Γ, $-\beta\sigma_D^2/2$, the energy barrier Γ decreases with the distribution of D. We perform KMCS in the range of $\beta = 50$–100, with $D_0 = 0.125$ at $|H| = 3.25$, and fit the data to Eq. (24) with fitting parameters Γ_0 and A with σ_D fixed (Table IV). For $\sigma_D = 0.0125$, the fitted values of Γ_0 and A agree with Eq. (24) within σ_D. For $\sigma_D = 0.025$, the agreement between the fitting and the AMC result is not as good as the case of $\sigma_D = 0.0125$ (still agreement within $2\sigma_D$). This is because the finite-size effect is more pronounced for larger σ_D [23].

The calculated average lifetime, Eq. (24), is valid only for $\Gamma > 0$, that is, $\beta < 2\Gamma_0/\sigma_D^2$. For example, for point b in region I-A, β must be less than 2800 for $D_0 = 0.125$, $\Gamma_0 = 0.375$, and $\sigma_D = 0.025$. (This value of β is too large to be realized numerically or experimentally.) Otherwise, Γ becomes negative and $\langle\tau\rangle$ becomes very short at an extremely low temperature, in contradiction to common sense. This contradiction occurs due to the approximation taken in order to obtain the analytical expression, Eq. (24). The approximation is that we replace a summation with an integral in calculating the average of the spin-flip probability over the Gaussian distribution, p_1. Using the Glauber dynamic, the expression of p_1 before the approximation (and before taking the $T \to 0$ limit) is

$$p_1 = \frac{1}{N}\sum_{i=1}^{N}\frac{1}{1+\exp\left[\beta(4 + D_i - |H|)\right]}, \tag{25}$$

where D_i is taken from the Gaussian distribution. In region I-A, Eq. (25) suggests that as $\beta \to \infty$, $p_1 \to 0$ and so $\langle\tau\rangle \to \infty$. Thus, there is no contradiction even at zero temperature. Another way to view the contradiction is that the Gaussian integral in $p_1 = \int f(D)\exp[-\beta(4 + D - |H|)]dD$ is not well defined for $\beta \to \infty$. In other words, when we rewrite p_1 as

$$p_1 = \left[\int_{-\infty}^{\infty}\frac{dD}{\sigma_D\sqrt{2\pi}}\exp\left(-\frac{\left\{D - \left(D_0 - \sigma_D^2\beta\right)\right\}^2}{2\sigma_D^2}\right)\right] \times \left[\exp\left(-\beta\Gamma_0 + \beta^2\sigma_D^2/2\right)\right], \tag{26}$$

the first bracket in the above expression equals 0 at $\beta = \infty$, but it equals unity otherwise. This subtlety in the analytic expression of $\langle\tau\rangle$ is applied to all regions and dynamics considered in Sec. V. Henceforth, all analytic forms of $\langle\tau\rangle$ shown in this paper are valid only for $\Gamma > 0$.

We now present our result for region II. A spin flip at site i represented by p_1 is independent of a spin flip at site j associated with p_2. Thus, as $T \to 0$, similarly to the case in region I-A, we can rewrite $p_1 p_2$ as

$$p_1 p_2 = \int_{-\infty}^{+\infty} f(D)e^{-\beta(4+D-|H|)}dD \times \int_{-\infty}^{+\infty} f(D')e^{-\beta(3+D'-|H|)}\,dD' \tag{27}$$
$$= \exp\left(-\beta\Gamma_0 + \beta^2\sigma_D^2\right). \tag{28}$$

Hence, using Eq. (13), the lifetime is given by

$$\langle\tau\rangle = A\exp[\beta\Gamma(\beta,H,D_0,\sigma_D)],$$
$$\Gamma(\beta,H,D_0,\sigma_D) = \Gamma_0(H,D_0) - \beta{\sigma_D}^2, \tag{29}$$

where $\Gamma_0(H,D_0) = 7 + 2D_0 - 2|H|$ and $A = 1/4$. We fit our KMCS data for $D_0 = 0.375$ at $|H| = 3.25$ (Fig. 5) to Eq. (29) with σ_D fixed. We find that $\Gamma_0 = 1.2503 \pm 1.33 \times 10^{-4}$ and $A = 0.2490 \pm 0.0021$ for $\sigma_D = 0.0125$ and that $\Gamma_0 = 1.2513 \pm 2.92 \times 10^{-4}$ and $A = 0.2300 \pm 0.0043$ for $\sigma_D = 0.025$. For $\sigma_D = 0.0125$, the fitted values are in good agreement with those using the AMC method, while

TABLE IV. Fitted values from our KMCS data and calculated values from the AMC method, using the Glauber dynamic with distributions of D centered at D_0 with σ_D at $|H| = 3.25$. For region I-A and the boundary, $\Gamma = \Gamma_0 - \beta\sigma_D^2/2$, and for region II, $\Gamma = \Gamma_0 - \beta\sigma_D^2$. Note that Γ_0 differs from Γ.

	Region I-A ($D_0 = 0.125$)	Boundary ($D_0 = 0.25$)	Region II ($D_0 = 0.375$)
$\sigma_D = 0.0125$	$\Gamma_0 = 0.8751 \pm 6.47 \times 10^{-5}$	$\Gamma_0 = 1.0002 \pm 6.54 \times 10^{-5}$	$\Gamma_0 = 1.2503 \pm 1.33 \times 10^{-4}$
	$A = 1.1225 \pm 0.0055$	$A = 1.2794 \pm 0.0064$	$A = 0.2490 \pm 0.0021$
$\sigma_D = 0.025$	$\Gamma_0 = 0.8746 \pm 9.15 \times 10^{-5}$	$\Gamma_0 = 0.9996 \pm 9.32 \times 10^{-5}$	$\Gamma_0 = 1.2513 \pm 2.92 \times 10^{-4}$
	$A = 1.1119 \pm 0.0078$	$A = 1.2688 \pm 0.0090$	$A = 0.2300 \pm 0.0043$
AMC method	$\Gamma_0 = 0.875$	$\Gamma_0 = 1$	$\Gamma_0 = 1.25$
	$A = 1.125$	$A = 1.28125$	$A = 0.25$

for $\sigma_D = 0.025$, there is a discrepancy between the fitted values and the AMC result due to the finite-size effect. The discrepancy for $\sigma_D = 0.025$ in this region is greater than that in region I-A, because the finite-size effect is enhanced in this region due to the use of two integrals in Eq. (27) instead of the one integral used in region I-A.

Finally, we show our result for the boundary. In the $T \to 0$ limit, $p_2 \to \int_{-\infty}^{+\infty} f(D)\Theta(D - |H| + 3))dD$ and $p_{20}^{+} \to \int_{-\infty}^{+\infty} f(D)\Theta(|H| - 3 - D)dD$, where $\Theta(x)$ is a Heaviside function. Applying them and p_1, discussed earlier, to Eq. (14), we find the lifetime as

$$\langle\tau\rangle = A\exp\left[\beta\Gamma(\beta,\sigma_D)\right], \quad \Gamma = \Gamma_0 - \frac{\beta\sigma_D^2}{2}, \tag{30}$$

where $\Gamma_0 = 1$ and $A = 41/32$. Fitting of our KMCS data (Fig. 6) provides that $\Gamma_0 = 1.0002 \pm 6.54 \times 10^{-5}$ and $A = 1.2794 \pm 0.0064$ for $\sigma_D = 0.0125$ and that $\Gamma_0 = 0.9996 \pm 9.32 \times 10^{-5}$ and $A = 1.2688 \pm 0.0090$ for $\sigma_D = 0.025$. Numerical uncertainties are consistently greater for $\sigma_D = 0.025$. For a summary, see Table IV.

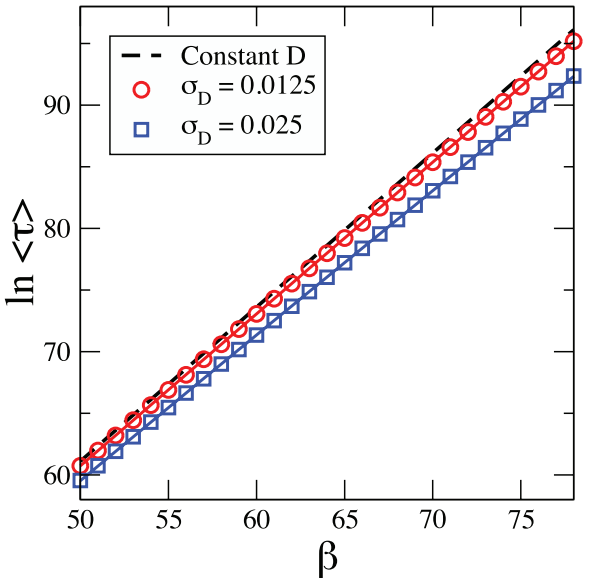

FIG. 5. (Color online) Simulated $\langle\tau\rangle$ vs β using the Glauber dynamic for distributions of D centered at $D_0 = 0.375$ (region II) with $\sigma_D = 0.0125$ and 0.025 for $L = 40$. Symbols indicate our data and solid curves are from the fitting. The lifetime for constant D is included.

B. Phonon-assisted dynamic

We discuss our result for region I-A. In this region, we rewrite Eq. (12) as

$$\langle\tau\rangle = \frac{1}{p_1} + \frac{p_{19}^{+}}{8p_1p_2}. \tag{31}$$

A spin flip at site i associated with p_{19}^{+} always occurs after a spin flip related to p_1 at the same site. A spin flip at site j associated with p_2 is independent of the spin slip at site i. Thus, taking into account the energy-dependent prefactor in the PA dynamic, we rewrite p_1, p_2, and p_1/p_{19}^{+} as follows:

$$p_1 = \int_{-\infty}^{\infty} f(D)(4 + D - |H|)^3 \times \exp[-\beta(4 + D - |H|)]\mathrm{d}D, \tag{32}$$

$$p_2 = \int_{-\infty}^{\infty} f(D')(-3 - D' + |H|)^3\mathrm{d}D', \tag{33}$$

$$\frac{p_1}{p_{19}^{+}} = \int_{-\infty}^{\infty} f(D)\exp[-\beta(4 + D - |H|)]\mathrm{d}D. \tag{34}$$

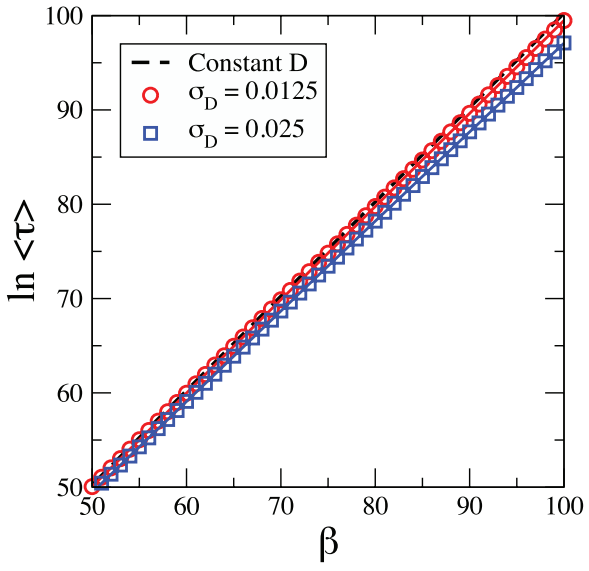

FIG. 6. (Color online) Simulated $\langle\tau\rangle$ vs β using the Glauber dynamic for distributions of D centered at $D_0 = 0.25$ (at the region boundary) with $\sigma_D = 0.0125$ and 0.025 for $L = 40$. Notations are the same as in Fig. 5.

TABLE V. Fitting of our KMCS data and the AMC result using the PA dynamic with distributions of D at $|H| = 3.25$. Γ_0 and A are fitted with fixed σ_D.

	Region I-A ($D_0 = 0.125$)	Boundary ($D_0 = 0.25$)	Region II ($D_0 = 0.375$)
$\sigma_D = 0.0125$	$\Gamma_0 = 0.8752 \pm 5.83 \times 10^{-5}$	$\Gamma_0 = 1.0098 \pm 2.12 \times 10^{-4}$	$\Gamma_0 = 1.2547 \pm 1.73 \times 10^{-4}$
	$A = 62.988 \pm 0.281$	$A = 23825 \pm 386$	$A = 42.843 \pm 0.477$
$\sigma_D = 0.025$	$\Gamma_0 = 0.8747 \pm 8.72 \times 10^{-5}$	$\Gamma_0 = 1.0063 \pm 8.28 \times 10^{-5}$	$\Gamma_0 = 1.2700 \pm 0.0002$
	$A = 57.293 \pm 0.382$	$A = 5318.3 \pm 33.6$	$A = 33.862 \pm 0.426$
AMC method	$\Gamma_0 = 0.875$	$\Gamma_0 = 1.00$	$\Gamma_0 \approx 1.25$
	$A = 63.629(\sigma_D = 0.0125)$	$A = 80212(\sigma_D = 0.0125)$	
	$A = 58.636(\sigma_D = 0.025)$	$A = 10027(\sigma_D = 0.025)$	

Using the above and keeping only leading terms, Eq. (31) becomes

$$\langle\tau\rangle = \exp\left[\beta\left(\Delta E_1^0 - \frac{1}{2}\sigma_D^2\beta\right)\right]\left[\frac{1}{\left(\Delta E_1^0\right)^3 - 3\left(\Delta E_1^0\right)^2\sigma_D^2\beta} + \frac{1}{8\left[\left(\Delta E_2^0\right)^3 + 3\Delta E_2^0\sigma_D^2\right]}\right], \tag{35}$$

where $\Delta E_1^0 = 4 + D_0 - |H|$ and $\Delta E_2^0 = -3 - D_0 + |H|$. Then, expanding the terms in the bracket up to σ_D^2 terms, we find

$$\langle\tau\rangle = A(\sigma_D)\exp[\beta\Gamma(\beta, H, D_0, \sigma_D)] = A(\sigma_D)\exp\left(\beta\Gamma_0 - \frac{1}{2}\beta^2\sigma_D^2\right), \tag{36}$$

$$A(\sigma_D) = A_0 - \frac{3\sigma_D^2}{8\left(\Delta E_2^0\right)^5} + O\left(\sigma_D^4\right), \tag{37}$$

$$\Gamma_0 = \Delta E_1^0 + \frac{3\sigma_D^2}{A\left(\Delta E_1^0\right)^4} + O\left(\sigma_D^4\right) \approx \Delta E_1^0, \tag{38}$$

where A_0 is the prefactor for constant D, Eq. (18), with D replaced by D_0. Interestingly, both the prefactor A and Γ_0 (not Γ) now depend on σ_D, in contrast to the Glauber dynamic. Considering that $0 < \Delta E_2 < \Delta E_1 < 1$ and $A_0 \gg 1$, we expect that prefactor A has a more significant dependence on σ_D than Γ_0. Fitting of our KMCS data (not shown) to Eq. (36) shows that $\Gamma_0 = 0.8752 \pm 5.83 \times 10^{-5}$ and $A = 62.988 \pm 0.281$ for $\sigma_D = 0.0125$ and that $\Gamma_0 = 0.8747 \pm 8.72 \times 10^{-5}$ and 57.293 ± 0.382 for $\sigma_D = 0.025$. Our fitting implies that the fitted value of A is indeed lower than A_0 (=65.4927) and that Γ_0 is close to that for constant D and for the Glauber dynamic. The fitted values of Γ_0 and A are close to the AMC result (Table V), but the agreement is not as good as that for the Glauber dynamic.

In region II, Eq. (13) does not provide an analytic form of $\langle\tau\rangle$ for the PA dynamic due to the energy-dependent prefactor in the dynamic. However, one can predict leading terms of Γ from p_1 and p_2. They are the same as those for the Glauber dynamic, Eq. (29). However, it is not possible to find an approximate analytic form for prefactor A in this case. Our fitting of the KMCS data (Fig. 7) to Eq. (29) shows that $\Gamma_0 = 1.2547 \pm 1.73 \times 10^{-4}$ and $A = 42.843 \pm 0.477$ for $\sigma_D = 0.0125$ and that $\Gamma_0 = 1.2700 \pm 0.0002$ and $A = 33.862 \pm 0.426$ for $\sigma_D = 0.025$. We also fit the data using three fitting parameters such as Γ_0, A, and σ_D (not listed). This fitting also consistently gives a much lower value of A than the value for constant D, $A = 64.512$. For $\sigma_D = 0.025$, the fitted value of A is almost half that for constant D. It is apparent that the value of A substantially decreases with increasing σ_D.

At the boundary, our KMCS data with distributions of D (Fig. 8) show a lifetime that is about 10 orders of magnitude shorter, at the low temperatures considered, than that for constant D. This is due to the absence of forbidden transitions. The metastable state can now relax through spin flips at sites with smaller values of D than D_0, where spin flips represented by p_2 are allowed or $\Delta E_2 \neq 0$, where $\Delta E_2 = 3 + D - |H|$. Note that $\Delta E_2 = 0$ at $D = D_0$. Since the energy barrier Γ is determined by the smallest magnetic anisotropy parameter within a distribution of D [23], we predict that the lifetime in this case obeys a form similar to that for region I-A with a distribution of D. At the boundary ($|H| = D_0 + 3$ and $0 < D_0 < 0.5$), the first term in Eq. (31) is negligible and only the second term significantly contributes to the lifetime. Across the boundary (varying D with fixed $|H|$), ΔE_2 changes its sign. Thus, in the $T \to 0$ limit, p_2, defined to be $\int_{-\infty}^{+\infty} f(D)(\Delta E_2)^3/(e^{\beta\Delta E_2} - 1)dD$, approximates $\int_{-\infty}^{|H|-3} f(D)(3 + D - |H|)^3 dD = \sqrt{2/\pi}\sigma_D^3$. Using this and

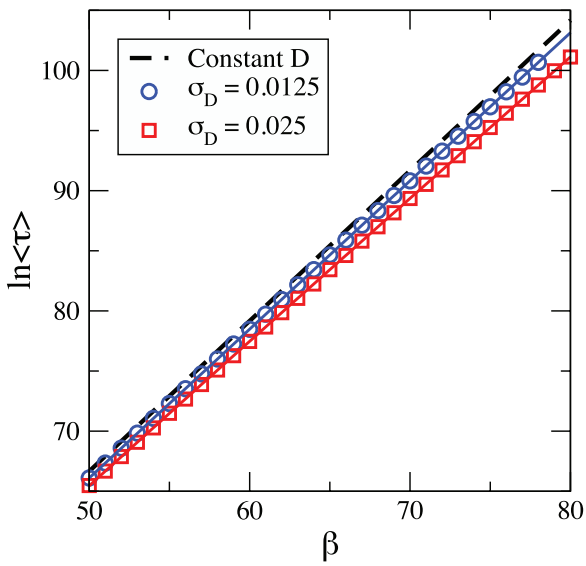

FIG. 7. (Color online) Simulated $\langle\tau\rangle$ vs β using the PA dynamic for Gaussian distributions of D centered at $D_0 = 0.375$ (region II). Notations are the same as in Fig. 5.

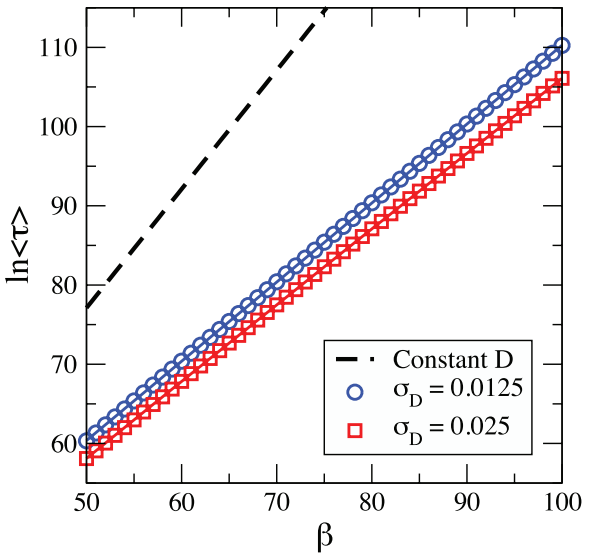

FIG. 8. (Color online) Simulated $\langle\tau\rangle$ vs β using the PA dynamic for Gaussian distributions at the boundary $D_0 = 0.25$. Notations are the same as in Fig. 5.

Eq. (34), we find that

$$\langle\tau\rangle = A(\sigma_D)\exp\left(\beta\Gamma_0 - \frac{1}{2}\sigma_D^2\beta^2\right), \tag{39}$$

$$A(\sigma_D) = \frac{\sqrt{\pi}}{8\sqrt{2}\sigma_D^3}, \quad \Gamma_0 = \Delta E_1^0 = 1, \tag{40}$$

where prefactor A also depends on σ_D. Fitting of our data in the range of $\beta = 50$–100 to Eq. (39) shows that $\Gamma_0 = 1.0098 \pm 2.12 \times 10^{-4}$ and $A = 23825 \pm 386$ for $\sigma_D = 0.0125$ and that $\Gamma_0 = 1.0063 \pm 8.28 \times 10^{-5}$ and $A = 5318.3 \pm 33.6$ for $\sigma_D = 0.025$. Our fitted value of Γ_0 is close to that using the AMC method, Eq. (39), and the fitted value of A decreases with increasing σ_D as predicted (Table V). However, the fitted value of A is much smaller than that derived from the AMC method for a given σ_D value. Strictly speaking, the prefactor $A(\sigma_D)$ in Eq. (40) is exact at $T = 0$. The temperature range in our KMCS may not be low enough to agree with $A(\sigma_D)$ in Eq. (40).

VI. CONCLUSION

We have investigated the relaxation of magnetization or the decay of the metastable state in the zero-temperature limit for the spin $S = 1$ square-lattice ferromagnetic BC model with distribution of magnetic anisotropy, using the Glauber and PA dynamics in two regions of different sizes of the critical droplet and at the boundary between the regions, within the single-droplet regime. Using the AMC method, we were able to predict the average relaxation time of magnetization or the average lifetime of the metastable state for both dynamics in most cases that we considered. The predicted lifetimes agree with those obtained from our KMCSs. We found that the average lifetime is governed by a modified Arrhenius law, where the energy barrier depends on the temperature, and it decreases with increasing standard deviation of the distribution of magnetic anisotropy. The amount of the decrease as a function of the standard deviation differs in different regions. At the boundary between the different regions, for the PA dynamic, the long lifetime of the metastable state caused by forbidden transitions (for constant magnetic anisotropy) can be dramatically lowered by introducing a small distribution of magnetic anisotropy. In addition, for the PA dynamic, a significant change in the prefactor A was found as a function of the standard deviation, in contrast to the Glauber dynamic. Since the two dynamics are affected differently by the distribution of magnetic anisotropy, studies of metastability with distribution of magnetic anisotropy can be used as a way to determine an underlying dynamic relevant to the system of interest.

ACKNOWLEDGMENTS

The authors were supported by NSF Grant Nos. DMR-0804665 and DMR-1206354.

APPENDIX: AVERAGE METASTABLE LIFETIME AT A LOWER MAGNETIC FIELD

We calculate an analytic form of the average lifetime in region IV-A confined by $(2 + D) < |H| < (3 - D)$ and $D > 0$ in Fig. 9, with the Glauber dynamic for constant D and distribution of D. We use the $s = 4$ AMC method with the

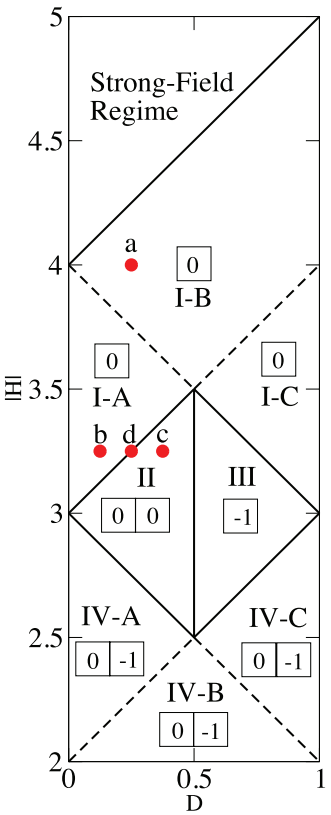

FIG. 9. (Color online) Crossover dynamic "phase" diagram for metastable decay for the square-lattice ferromagnetic BC model with $0 < D < 1$ in the zero-temperature limit (for constant D). Four regions—I, II, III, and IV—within the single-droplet regime are specified with illustrated critical droplets. Notation is the same as in Fig. 1.

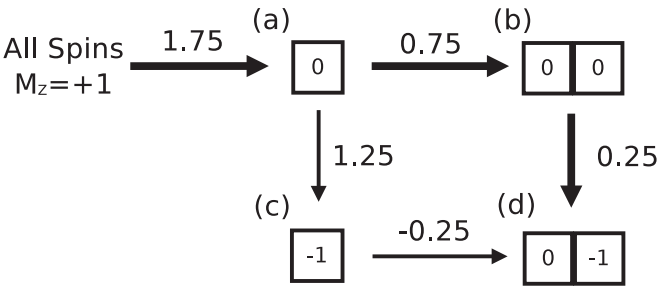

FIG. 10. Schematic of relaxation pathways for region IV-A shown in Fig. 9. Each spin configuration shows only flipped spin projections from the initial state (all spins with $M_z = +1$). Bold arrows represent the most probable relaxation pathway. Numbers next to or above the arrows represent ΔE between the corresponding states for $|H| = 2.5$ and $D = 0.25$.

following four transient states (and eight absorbing states): the three transient states in the $s = 3$ AMC method (discussed in Sec.IV) and the state of two nearest-neighbor sites with $M_z = 0$ and $M_z = -1$ [Fig. 10(d)]. The most probable relaxation pathway in this region is shown by bold arrows in Fig. 10. The exit time from the transient subspace or $\langle\tau\rangle$ as a function of $|H|$, D, T, and N is given by

$$
\begin{aligned}
\langle\tau\rangle &= \frac{A_1 + B_1 + C_1 + D_1}{p_1(A_2 + B_2 + C_2 + D_2)},\\
A_1\big(p_1^3\big) &= 4p_1^3(N-8)^2(2N-5),\\
A_2\big(p_1^3\big) &= 4p_1^3(N-8)^2(N-5),\\
B_1\big(p_1^2\big) &= 2p_1^2(N-8)[2p_2(13N-77)+(2N-5)\\
&\quad\times\{2(3p_3+p_{11}+p_{20}^{+}+p_{20}^{-})+p_{21}^{+}+p_{21}^{-}\}\\
&\quad+(N-8)(p_{19}^{+}+p_{19}^{-})+26Np_2],\\
B_2\big(p_1^2\big) &= 2p_1^2(N-8)[2p_2(13N-77)+(N-5)\\
&\quad\times\{2(3p_3+p_{11}+p_{20}^{+}+p_{20}^{-})+p_{21}^{+}+p_{21}^{-}\}\\
&\quad+(N-8)p_{19}^{-}],\\
C_1(p_1) &= p_1\big[168p_2^2(2N-9)+2(2N-5)\{2p_{20}^{+}(p_{11}+3p_2)\\
&\quad+(p_{20}^{+}+p_{20}^{-})(6p_3+p_{21}^{+}+p_{21}^{-})\}+(p_{19}^{+}+p_{19}^{-})\\
&\quad\times(N-8)\{6(3p_2+p_3)+2(p_{11}+p_{20}^{+}+p_{20}^{-})\\
&\quad+p_{21}^{+}+p_{21}^{-}\}+4p_2\{(10N-31)\\
&\quad\times(6p_3+2p_{11}+p_{21}^{+}+p_{21}^{-})+p_{20}^{-}(14N-47)\}\big],\\
C_2(p_1) &= p_1\big[216p_2^2(N-7)+2(N-5)\{2p_{20}^{+}(p_{11}+3p_2)\\
&\quad+(p_{20}^{+}+p_{20}^{-})(6p_3+p_{21}^{+}+p_{21}^{-})\}+p_{19}^{-}(N-8)\\
&\quad\times\{6(3p_2+p_3)+2(p_{11}+p_{20}^{+}+p_{20}^{-})\\
&\quad+p_{21}^{+}+p_{21}^{-}\}+4p_2\{(5N-31)(6p_3+2p_{11}+p_{21}^{+}\\
&\quad+p_{21}^{-})+p_{20}^{-}(7N-47)\}\big],\\
D_1 &= 2p_{11}\big\{48p_2^2+(p_{19}^{+}+p_{19}^{-})(6p_2+p_{20}^{+})\big\}\\
&\quad+\big\{48p_2^2+8p_2p_{20}^{-}+(p_{19}^{+}+p_{19}^{-})(6p_2+p_{20}^{+}\\
&\quad+p_{20}^{-})\big\}(6p_2+6p_3+p_{21}^{+}+p_{21}^{-}),\\
D_2 &= 2p_{11}\big\{48p_2^2+2p_{19}^{-}(6p_2+p_{20}^{+})\big\}+\big\{48p_2^2+8p_2p_{20}^{-}\\
&\quad+p_{19}^{-}(6p_2+p_{20}^{+}+p_{20}^{-})\big\}(6p_2+6p_3+p_{21}^{+}+p_{21}^{-}).
\end{aligned}
\tag{A1}
$$

1. Constant magnetic anisotropy parameter

In the $T \to 0$ limit, p_{21}^{+} approaches 0, and p_3, p_{10}, p_{11}, p_{19}^{+}, p_{20}^{+}, and p_{21}^{-} approach unity. p_1 approaches $\exp[-(4+D-|H|)]$ and p_2 approaches $\exp[-(3+D-|H|)]$. p_{19}^{-} approaches $\exp[-(4-D-|H|)]$ and p_{20}^{-} approaches $\exp[-(3-D-|H|)]$. In addition, in region IV-A, $p_1 \ll p_{19}^{-} \ll p_2 p_{20}^{-}$, and so A_1, A_2, B_1, B_2, C_1, and C_2 approach 0 as $T \to 0$. Thus, Eq. (A1) is reduced to

$$
\langle\tau\rangle = \frac{D_1}{p_1 D_2}, \tag{A2}
$$

and it can be further approximated to

$$
\begin{aligned}
\langle\tau\rangle &= \frac{9}{56}(p_1 p_2 p_{20}^{-})^{-1}\\
&= \frac{9}{56}\exp[\beta(10+D-3|H|)].
\end{aligned}
\tag{A3}
$$

2. Distribution of the magnetic anisotropy parameter

With a Gaussian distribution $f(D)$ of D, using the same analogy as before (Sec. V A), for $T \to 0$, we can compute the average of the probability $p_1 p_2 p_{20}^{-}$ over $f(D)$, such as

$$
\begin{aligned}
p_1 p_{20}^{-} p_2 &= \int_{-\infty}^{+\infty} f(D) e^{-\beta(4+D-|H|)}\, e^{-\beta(3-D-|H|)}\, dD\\
&\quad\times\int_{-\infty}^{+\infty} f(D') e^{-\beta(3+D'-|H|)}\, dD',
\end{aligned}
\tag{A4}
$$

where $p_1 p_{20}^{-}$ does not give a dependence on σ_D. We can rewrite $p_1 p_{20}^{-} p_2$ as

$$
p_1 p_{20}^{-} p_2 = \exp\left(-\beta\Gamma_0 + \frac{\beta^2\sigma_D^2}{2}\right). \tag{A5}
$$

Hence, using the above equation, we find that the average lifetime is

$$
\begin{aligned}
\langle\tau\rangle &= A\exp[\beta\Gamma(\beta,H,D_0,\sigma_D)],\\
\Gamma(\beta,H,D_0,\sigma_D) &= \Gamma_0(H,D_0) - \frac{\beta{\sigma_D}^2}{2},
\end{aligned}
\tag{A6}
$$

where $\Gamma_0(H,D_0) = 10 + D_0 - 3|H|$ and $A = 9/56$. The expression of Γ is valid only for $\beta < 2\Gamma_0/\sigma_D^2$, as discussed earlier. The prefactor is the same as that for the constant D case, and the dependence of σ_D on Γ is the same as that for region I and the boundary discussed in the main text.

[1] S. Sun, C. B. Murray, D. Weller, L. Folks, and A. Moser, Science **287**, 1989 (2000).

[2] S. H. Sun, Adv. Mater. **18**, 393 (2006); B. D. Terris and T. Thomson, J. Phys. D: Appl. Phys. **38**, R199 (2005).

[3] A. K. Gupta and M. Gupta, Biomat. **26**, 3995 (2005).
[4] Y. L. Wang, W. Li, S. Y. Zhou, D. L. Kong, H. S. Yang, and L. X. Wu, Chem. Comm. **47**, 3541 (2011).
[5] J. E. Mertzman, S. Kar, S. Lofland, T. Fleming, E. Van Keuren, Y. Y. Tong, and S. L. Stoll, Chem. Comm., 788 (2009).
[6] D. Alloyeau, G. Prévot, Y. Le Bouar, T. Oikawa, C. Langlois, A. Loiseau, and C. Ricolleau, Phys. Rev. Lett. **105**, 255901 (2010).
[7] Y. Bao, A. B. Pakhomov, and K. M. Krishnan, J. Appl. Phys. **97**, 10J317 (2005).
[8] S. B. Choe and S. C. Shin, Phys. Rev. B **65**, 224424 (2002); M. Y. Im, D. H. Kim, and S. C. Shin, *ibid.* **72**, 132416 (2005).
[9] R. Belhi, A. Adanlété Adjanoh, J. Vogel, M. Ayadi, and K. Adbelmoula, J. Appl. Phys. **108**, 093924 (2010).
[10] I. Volkov, M. Chukharkin, O. Snigirev, A. Volkov, S. Tanaka, and C. Fourie, J. Nanopart. Res. **10**, 487 (2008).
[11] S.-P. Yu, Y.-H. Liu, A.-C. Sun, and J.-H. Hsu, J. Appl. Phys. **106**, 103905 (2009).
[12] O. Crisan, K. von Haeften, A. M. Ellis, and C. Binns, Nanotechnology **19**, 505602 (2008).
[13] S. Yoon, J. Magn. Magn. Mater. **324**, 2620 (2012).
[14] M. Blume, Phys. Rev. **141**, 517 (1966).
[15] H. W. Capel, Physica **32**, 966 (1966).
[16] P. Zhang, F. Zuo, F. K. Urban, A. Khabari, P. Griffiths, and A. Hosseini-Tehrani, J. Magn. Magn. Mater. **225**, 337 (2001).
[17] Y. I. Kim, D. Kim, and C. S. Lee, Physica B-Cond. Matt. **337**, 42 (2003).
[18] P. Politi, A. Rettori, F. Hartmann-Boutron, and J. Villain, Phys. Rev. Lett. **75**, 537 (1995)
[19] M. N. Leuenberger and D. Loss, Phys. Rev. **61**, 1286 (2000).
[20] E. M. Chudnovsky, D. A. Garanin, and R. Schilling, Phys. Rev. B **72**, 094426 (2005).
[21] C. Coulon, R. Clérac, L. Lecren, W. Wernsdorfer, and H. Miyasaka, Phys. Rev. B **69**, 132408 (2004).
[22] J. I. Kishine, T. Watanabe, H. Deguchi, M. Mito, T. Sakai, T. Tajiri, M. Yamashita, and H. Miyasaka, Phys. Rev. B **74**, 224419 (2006).
[23] Y. Yamamoto and K. Park, Phys. Rev. B **84**, 094415 (2011).
[24] R. J. Glauber, J. Math. Phys. **4**, 294 (1963).
[25] P.-A. Martin, J. Stat. Phys. **16**, 149 (1977).
[26] N. Klinduhov, D. Chernyshov, and K. Boukheddaden, Phys. Rev. B **81**, 094408 (2010).
[27] N. Metropolis, A. Rosenbluth, M. Rosenbluth, A. Teller, and E. Teller, J. Chem. Phys. **21**, 1087 (1953).
[28] P. A. Rikvold and M. Kolesik, J. Stat. Phys. **100**, 377 (2000).
[29] K. Park, P. A. Rikvold, G. M. Buendía, and M. A. Novotny, Phys. Rev. Lett. **92**, 015701 (2004).
[30] G. M. Buendía, P. A. Rikvold, M. Kolesik, K. Park, and M. A. Novotny, Phys. Rev. B **76**, 045422 (2007).
[31] K. Park, Phys. Rev. B **77**, 104420 (2008).
[32] T. Meunier, I. T. Vink, L. H. Willems van Beveren, K.-J. Tielrooij, R. Hanson, F. H. L. Koopens, H. P. Tranitz, W. Wegscheider, L. P. Kouwenhoven, and L. M. K. Vandersypen, Phys. Rev. Lett. **98**, 126601 (2007).
[33] A. B. Bortz, M. H. Kalos, and J. L. Lebowitz, J. Comput. Phys. **17**, 10 (1975).
[34] M. A. Novotny, Phys. Rev. Lett. **75**, 1424 (1995).
[35] M. A. Novotny, in *Annual Reviews of Computational Physics IX*, edited by D. Stauffer, (World Scientific, Singapore, 2001), pp. 153–210; arXiv:cond-mat/0109182v1.
[36] K. Yosida, *Theory of Magnetism* (Springer-Verlag, Heidelberg, Germany, 1996), Chap. 3.
[37] R. da Silva, N. A. Alves, and J. R. Drugowich de Felício, Phys. Rev. E **66**, 026130 (2002).
[38] Y. Tanaka and N. Uryû, J. Phys. Soc. Jpn. **50**, 1140 (1981).
[39] H. Polat, Ü. Akinci, and Í. Sökmen, Phys. Status Solidi B **240**, 189 (2003).
[40] A. Du, Y. Q. Yü, and H. J. Liu, Physica A **320**, 387 (2003).
[41] P. A. Rikvold, H. Tomita, S. Miyashita, and S. W. Sides, Phys. Rev. E **49**, 5080 (1994).
[42] H. L. Richards, S. W. Sides, M. A. Novotny, and P. A. Rikvold, J. Magn. Magn. Mater. **150**, 37 (1995).
[43] V. A. Shneidman and G. M. Nita, Phys. Rev. Lett. **89**, 025701 (2002).
[44] V. A. Shneidman, J. Stat. Phys. **112**, 293 (2003).
[45] E. N. M. Cirillo and E. Olivieri, J. Stat. Phys. **83**, 473 (1996).
[46] G. E. P. Box and M. E. Muller, Ann. Math. Stat. **29**, 610 (1958).
[47] M. D. Grynberg and R. B. Stinchcombe, arXiv:1303.1771.